Study of stability and thermo-magnetic response of MnCoFeGeSi mechanically alloyed systems

A. Vidal-Crespo [1], R. Caballero-Flores [2], J.J. Ipus [*,3], J.S. Blázquez [4], F.J. Romero [5], C.F. Conde [6]

Departamento Física de la Materia Condensada, ICMSE-CSIC, Universidad de Sevilla, P.O. Box 1065, 41080 Sevilla, Spain

ARTICLE INFO

ABSTRACT

Amorphous precursors with the composition $MnCo_{0.8}Fe_{0.2}Ge_{1-x}Si_x$, where $x = 0.2, 0.3, 0.4$, and 0.6, were obtained through mechanical alloying. These precursors were subsequently subjected to different thermal treatments, resulting in the formation of the austenite Ni_2In-type structure for $x \leq 0.4$. For the highest Si content ($x = 0.6$), this phase coexists with the martensite TiNiSi-type structure without apparent partitioning of the elements at the nanoscale. These structures remain stable up to their melting points, but subsequent melting processes exhibit differences compared to the initial solidification at a cooling rate of -20 K/min. The magnetocaloric effect was investigated through thermomagnetic and heat capacity measurements and simulated using the Arrott-Noakes equation of state, revealing the presence of a distribution of Curie temperatures. Despite the absence of a martensitic transformation, these alloys exhibit a significant magnetocaloric response, which increases as the precursor system's amorphization (i.e., homogenization) is enhanced.

1. Introduction

The MnCoGe system exhibits a magnetostructural transition at approximately 420 K, transitioning from a low-temperature orthorhombic structure (martensitic TiNiSi-type structure, Pnma space group) to a high-temperature hexagonal structure (austenitic Ni_2In-type structure, P6$_3$/mmc space group) [1]. For the stoichiometric composition, both phases, martensite and austenite, exhibit ferromagnetic behavior with Curie temperatures of 276 K and 355 K [2], respectively. Such systems demonstrate intriguing properties, including a substantial magnetocaloric effect (MCE) and giant negative thermal expansion [3, 4].

While the magnetic and structural transitions are decoupled in the MnCoGe composition [1], this magnetostructural transition can be influenced by compositional variations [5–11], introduction of vacancies [12], and application of external pressure [13]. Furthermore, it can be suppressed in samples produced through mechanical alloying, even after annealing processes, leading to the stabilization of the austenite phase at elevated temperatures [14].

In this study, we explore the $MnCo_{0.8}Fe_{0.2}Ge_{1-x}Si_x$ ($x = 0.2, 0.3, 0.4$, and 0.6) systems, which are synthesized in two steps: first, by creating a precursor homogeneous system through mechanical alloying, and subsequently subjecting it to a thermal treatment to produce the desired crystalline samples. Typically, these systems are synthesized via arc-melting [1], and extensive subsequent thermal treatments are required to achieve the desired phases.

Moreover, our work highlights the significant advantage of mechanical alloying, which requires a considerably shorter thermal treatment at a lower annealing temperature (e.g., 20 min vs. 72 h and 723 K vs. 1123 K) [14]. We also investigate the microstructure and thermal stability of these systems up to the melting process. The magnetic entropy change is determined through temperature and field-dependent magnetization curves and simulated using the Arrott-Noakes equation of state. The temperature-dependent specific heat at zero applied field allows us to estimate a lower limit for the adiabatic temperature change in alloys that exhibit the highest magnetocaloric response ($x = 0.4$) and

* Corresponding author.
  E-mail address: jhonipus@us.es (J.J. Ipus).

[1] 0000-0002-6633-9459
[2] 0000-0001-9736-4422
[3] 0000-0002-5402-6164
[4] 0000-0003-2318-5418
[5] 0000-0002-4551-0050
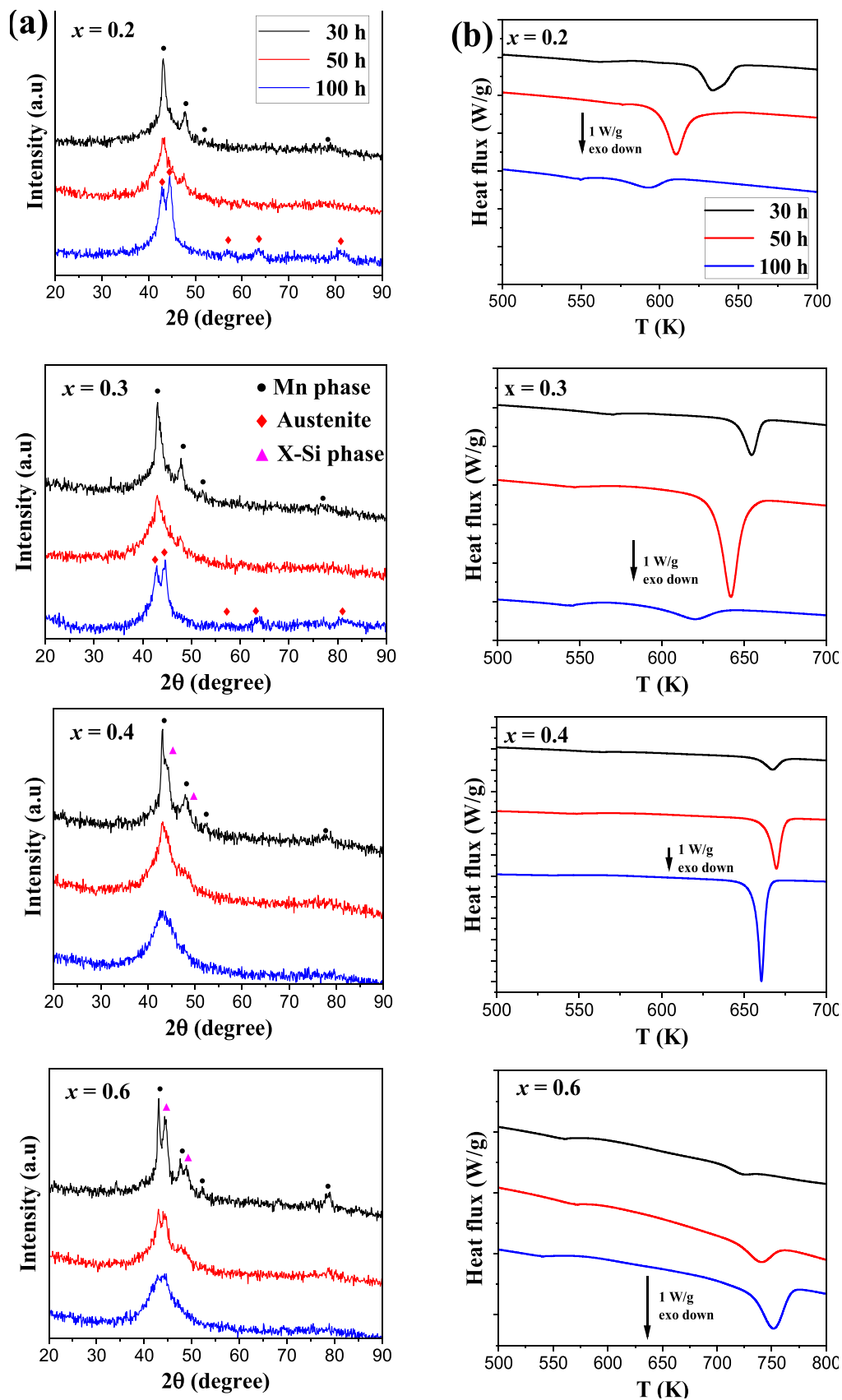[6] 0000-0003-4156-6249

Fig. 1. Column (a) XRD patterns of the mechanically alloyed precursor powders for each composition after different milling times. Symbols indicate the Bragg's positions of each phase cited in the legend. **Column (b)** DSC scans at 20 K/min from room temperature to 973 K as a function of milling time. The arrow indicates the magnitude and nature of the transformation. X axes are set to the displayed range for better observation. Y axes are the same for better comparison.

Table 1

Parameters from DSC scans as a function of milling time.

Si content	Temperature peak, $T_{pk} \pm 1$ (K)			Transformation heat, q (W/g)		
	30 h	50 h	100 h	30 h	50 h	100 h
$x = 0.2$	634	610	592	-37 ± 4	-59 ± 4	-15 ± 1
$x = 0.3$	655	642	620	-28 ± 1	-107 ± 1	-24 ± 1
$x = 0.4$	667	670	660	-18 ± 1	-56 ± 2	-87 ± 4
$x = 0.6$	723	739	751	-8 ± 1	-26 ± 3	-57 ± 1

the coexistence of martensite and austenite phases ($x = 0.6$).

2. Experimental

Precursor samples were created from high-purity elements ($> 99\%$). Five-gram mixtures of the nominal composition MnCo$_{0.8}$Fe$_{0.2}$Ge$_{1-x}$Si$_x$, with $x = 0.2$, 0.3, 0.4, and 0.6, were prepared using a Fritsch Pulverisette Vario 4 planetary mill equipped with 10 mm diameter steel balls and 80 cm^3 hardened steel vials as milling media. The ball-to-powder mass ratio was 10:1, and the ratio between the rotational velocity of the vials and the main disk was -2. Powder manipulation took place within a Saffron Omega glovebox under a controlled atmosphere of argon, with oxygen and humidity levels maintained below 100 ppm and 20 ppm, respectively.

In the subsequent sections, we will distinguish between these precursor samples and the final samples, which refer to those precursor samples subjected to a thermal treatment. This treatment involved heating at a rate of 20 K/min from room temperature up to 723 K (for $0.2 \leq x \leq 0.4$) or up to 883 K (for $x = 0.6$) using a differential scanning calorimeter (DSC) DSC7 Perkin-Elmer operating under an argon flow.

Structural analysis was performed using X-ray diffraction (XRD) with a powder diffractometer D8 Advance A25 at room temperature, employing Cu-K$_\alpha$ radiation. Phase identification was conducted using DIFFRAC.EVA software (version 4.1, Bruker), and Rietveld refinement was carried out with DIFFRAC.TOPAS software (version 6.0, Bruker). Transmission electron microscopy (TEM) was conducted on powder samples using a FEI Talos S200 microscope operating at 200 kV. The chemical composition of the samples was analyzed through X-ray fluorescence (XRF) using EAGLE III X-ray microfluorescence equipment with a Rh anticathode, and energy-dispersive X-ray spectroscopy (EDS) was employed in TEM analysis using scanning transmission mode (STEM) with a high-angle annular dark field (HAADF) detector. For TEM sample preparation, powder samples were initially spread on a porous copper grid and then blew with pressurized air and placed in a region with a magnetic field to remove any loosely adhered powder previous to put into the microscope.

To prevent the mobility of loose powder during magnetic and thermal characterization, powder samples were compressed using a hydrostatic press, applying a force of 2 tons at room temperature to produce disks approximately 5 mm in diameter.

Thermal stability tests were conducted using a DSC7 Perkin-Elmer calorimeter, covering the temperature range from room temperature up to 973 K. Additionally, a SDT Q600 equipment from TA Instruments was used, covering a range up to 1673 K, with a controlled argon atmosphere. In both cases, a heating rate of 20 K/min was applied. Magnetic properties were measured using a Lakeshore 7407 Vibrating Sample Magnetometer (VSM) with a maximum applied field of $\mu_0 H = 1.5$ T. Isothermal magnetization curves were obtained over a temperature range from 150 K to 400 K, with different temperature increments determined by the phase transition temperatures. Magnetic entropy change was calculated from isothermal magnetization curves using the Maxwell relation and was performed using the Magnetocaloric Effect
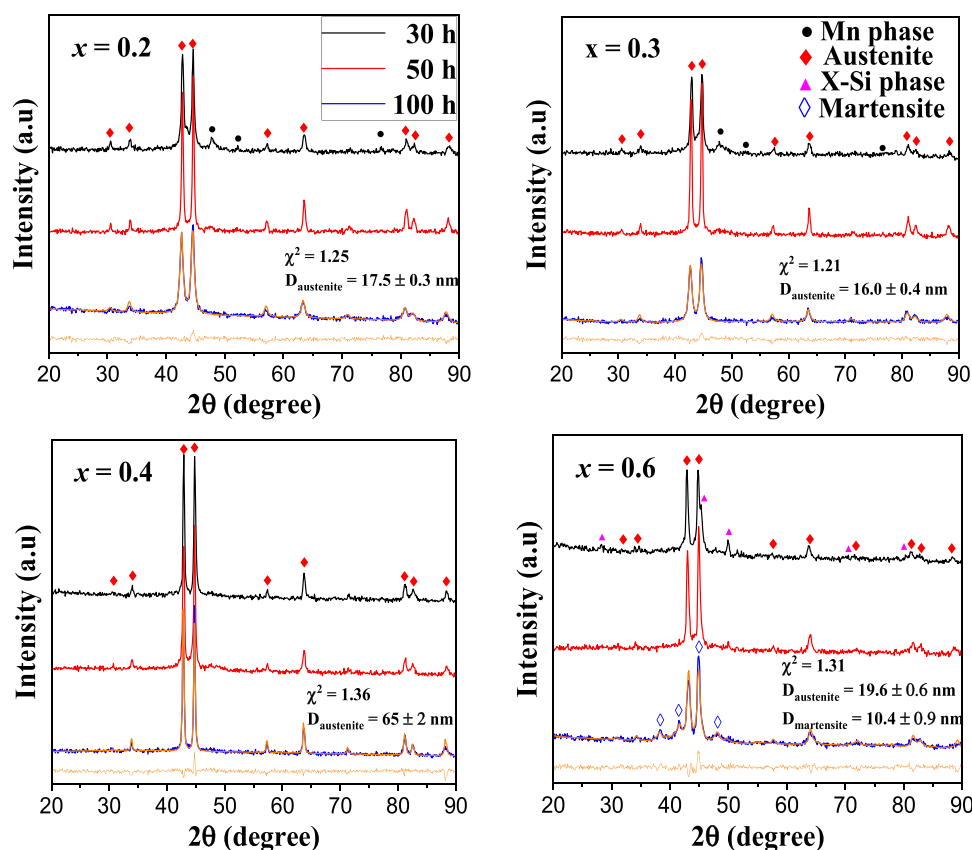

Fig. 2. XRD patterns of samples heated from room temperature up to 723 K (x = 0.2, 0.3 and 0.4) and 883 K (x = 0.6) at 20 K/min as a function of milling time. For 100 h, the experimental data are shown in blue, and the Rietveld fittings are shown in orange. The differences between the experimental data and the Rietveld fittings are shown in orange below each experimental pattern. **D** indicates the crystal size and χ^2 the goodness of fit.
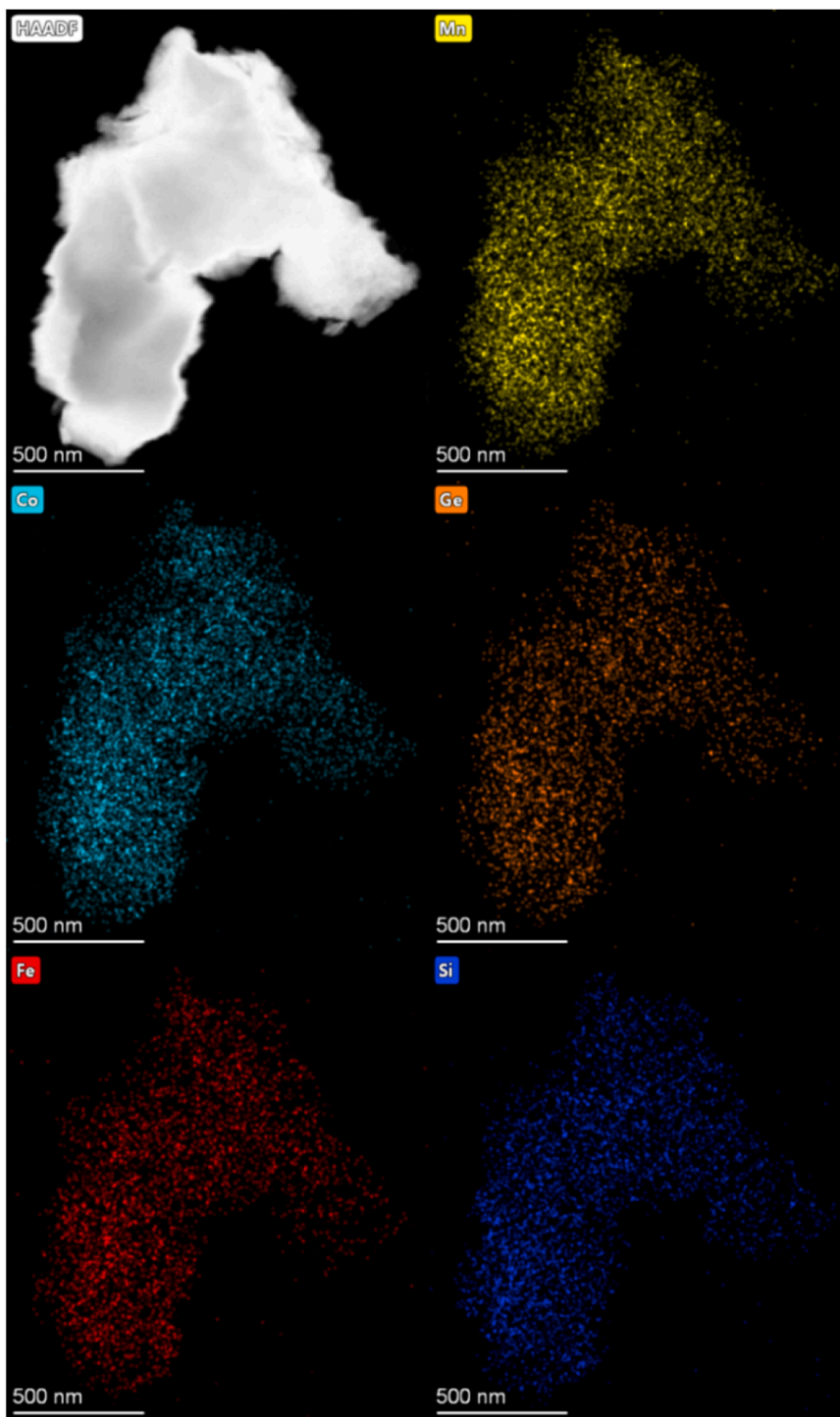
Fig. 3. STEM-EDS images of the sample with x = 0.6 milled 100 h and heated from room temperature up to 883 K at 20 K/min (Mn: yellow, Co: cyan, Ge: orange, Fe: red, Si: blue).

Analysis program [15]. It was also simulated using the Arrott-Noakes equation of state.

Specific heat measurements were carried out using the heat capacity option of a commercial Quantum Design Physical Property Measurement System, covering the temperature range from 150 K to 390 K. This calorimeter determines the heat capacity of a sample by controlling heat flow while monitoring the resulting temperature change. When it is assumed that the heat capacity remains constant during the heat pulse, it can be obtained by fitting the temperature evolution according to the solution of the two-tau model [16,17].

Mass measurements for these experiments were conducted using a Mettler Toledo XP 26 microbalance with a precision of 0.001 mg.

3. Results

3.1. Structural characterization

In Fig. 1a (left column), XRD patterns are depicted as a function of milling time (30 h, 50 h, and 100 h) for each composition. The patterns reveal the coexistence of multiple phases (Mn phase, austenitic phase,

Table 2
Composition analysis of samples.

Si content	Technique	Atomic concentration of elements (at%)				
		Mn	Co	Fe	Ge	Si
$x = 0.2$	XRF	31.2	27.3	6.7	28.2	6.6*
	EDS	33.9	26.2	7.0	27.1	5.8
$x = 0.3$	XRF	31.2	27.3	7.0	24.5	10.0*
	EDS	34.4	25.9	8.1	22.5	9.1
$x = 0.4$	XRF	31.4	28.0	6.4	20.8	13.4*
	EDS	37.2	26.1	7.8	21.5	7.4
$x = 0.6$	XRF	31.0	28.3	6.4	14.3	20.0*
	EDS	35.0	25.5	8.0	13.6	17.9

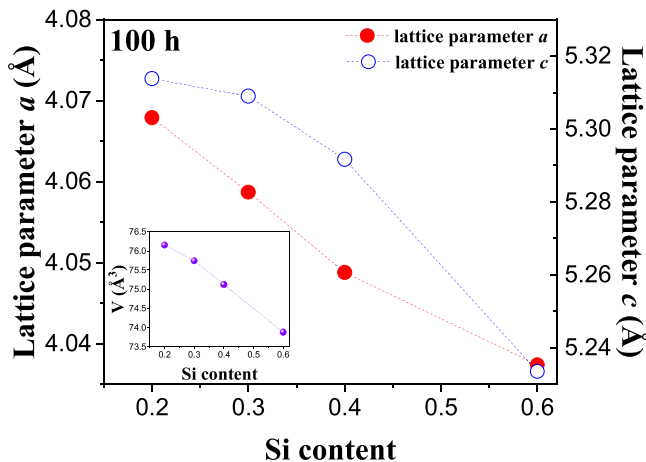* Nominal Si content is imposed for XRF.

Fig. 4. Lattice parameters evolution as a function of the Si content for the austenitic phase of final samples obtained from Rietveld fittings. Inset shows the evolution of austenite cell volume as a function of the Si content.

and X-Si phases, where X could be Fe, Co, or Mn) at each milling time. According to the Miedema model [18], although MnSi would be more favorable than others, the diffraction peaks suggest that CoSi and FeSi phases are the most probable. In this case, the CoSi phase exhibits the highest formation enthalpy value among the aforementioned phases. For $x = 0.2$ and 0.3, following 30 h of milling, the α-Mn phase (with the $I\bar{4}3m$ space group) persists, alongside the development of an amorphous phase during the milling process. A detailed investigation of this amorphous phase as a function of milling time can be found in the reference [19] for $x = 0$. Furthermore, for $x = 0.4$ and 0.6, after 30 h of milling, the presence of the X-Si phase (with the $P2_13$ space group) is observed, which is attributed to the increased Si content. As milling time is extended to 100 h, for $x = 0.2$ and 0.3, a recrystallization process occurs, leading to the formation of an austenitic hexagonal phase (with the $P6_3/mmc$ space group). This phenomenon aligns with similar compositions previously studied by the authors [14,20]. However, for $x = 0.4$ and 0.6, after 100 h of milling, the recrystallization process is absent, and mechanical amorphization continues to progress.

In Fig. 1b (right column), the DSC scans are presented at a heating rate of 20 K/min, ranging from room temperature to 973 K, as a function of milling time for each composition. For all compositions, these scans reveal a crystallization process occurring after heating to a specific temperature. These irreversible processes result in the formation of more stable phases compared to those obtained through mechanical alloying. Detailed parameters of these exothermic processes, including peak temperature and total transformation heat, are provided in Table 1.

As a result, it is evident that an increase in milling time corresponds to a higher degree of amorphization. However, for alloys with $x = 0.2$ and 0.3, the progress of amorphization is interrupted by a recrystallization process, consistent with the findings from the DSC results (see

Fig. 1, column b). In fact, for samples with $x = 0.2$ and 0.3 milled for 50 h, the crystallization enthalpy values are greater than those of samples milled for 100 h ($q_{50} > q_{100}$). On the other hand, for $x = 0.4$ and 0.6, the 100-hour milled samples exhibit a higher amorphous fraction compared to those milled for 50 h, a trend corroborated by the crystallization data presented in Table 1 ($q_{50} < q_{100}$).

Fig. 2 displays the XRD patterns of the final samples, which underwent the heat treatments described in the experimental section, following the crystallization events detected by DSC (as shown in Fig. 1b), for each composition. For $x = 0.2$ and 0.3, after 30 h of milling, both the austenitic hexagonal phase and α-Mn phase are discernible. In the case of $x = 0.6$, the final samples exhibit the austenitic hexagonal phase alongside the X-Si phase. Notably, for $x = 0.2$, 0.3, and 0.4, after 100 h of milling, the austenitic hexagonal phase re-emerges. In contrast, for $x = 0.6$, the martensitic orthorhombic phase (with a *Pnma* space group) appears in coexistence with the austenitic hexagonal phase.

Rietveld fittings provide lattice parameters and crystal size information for each identified phase in the final samples. In Fig. 2, it can be observed that the sample with $x = 0.4$ exhibits the largest crystal size, D = 65 ± 2 nm, whereas the other samples display a similar crystal size for the austenitic phase, with values of D = 17.5 ± 0.3 nm, 16.0 ± 0.4 nm, and 19.6 ± 0.6 nm for $x = 0.2$, 0.3, and 0.6, respectively. Additionally, for $x = 0.6$, both the austenitic and martensitic phases coexist, with the latter having a crystal size of D = 10.4 ± 0.9 nm and lattice parameters of a = 5.700 ± 0.008 Å, b = 3.786 ± 0.005 Å, and c = 7.091 ± 0.014 Å.

Fig. 3 presents a STEM image and the corresponding EDS maps for the final sample with $x = 0.6$. Notably, the sample exhibits homogeneity at the sub-micron scale, with no discernible nanometer-sized regions showing an enrichment in any specific element.

This fact is consistent across all the samples analyzed in this study, although they are not shown here. However, it is particularly noteworthy in the case of the $x = 0.6$ sample milled for 100 h, as it exhibited the coexistence of two phases (martensitic orthorhombic and austenitic hexagonal phases), as discussed previously. To confirm the chemical compositions of the samples, XRF and EDS analyses were performed, and the results are summarized in Table 2. Notably, no significant deviations were observed with respect to the nominal compositions. However, it is worth noting that the measurement of Si content is more challenging due to the element's light character, and compositional deviations, particularly for the sample with $x = 0.4$, were found to be around 45%.

Fig. 4 illustrates the evolution of lattice parameters for the austenitic phase as a function of Si content. It is evident that the cell volume of the austenitic phase decreases with increasing Si content, and this trend remains consistent even for $x = 0.6$. This observation aligns with the homogeneous composition observed at the nanoscale, even in the case of this two-phase system, as depicted in Fig. 3.

3.2. Structural stability

To assess the structural stability of the final samples beyond the operational limit of the Perkin-Elmer calorimeter (973 K, as described in the experimental section), melting experiments were conducted using an SDT Q600 DSC equipment. The samples employed for these experiments were those milled for 100 h. The experiments consisted of heating and cooling cycles between room temperature and 1673 K, with a heating/cooling rate of 20 K/min, as described in Fig. 5. Initially, in the temperature range of 600 K to 800 K, a crystallization process is observed, leading to the development of the phases identified in Fig. 2. No additional transformation events are observed beyond 973 K. Consequently, in this state, all samples exhibit a single asymmetric endothermic peak during melting, with the exception of $x = 0.4$, where a small peak is observed at a slightly lower temperature. Subsequent cooling from the molten state down to room temperature at 20 K/min reveals no evidence of martensitic transformation.

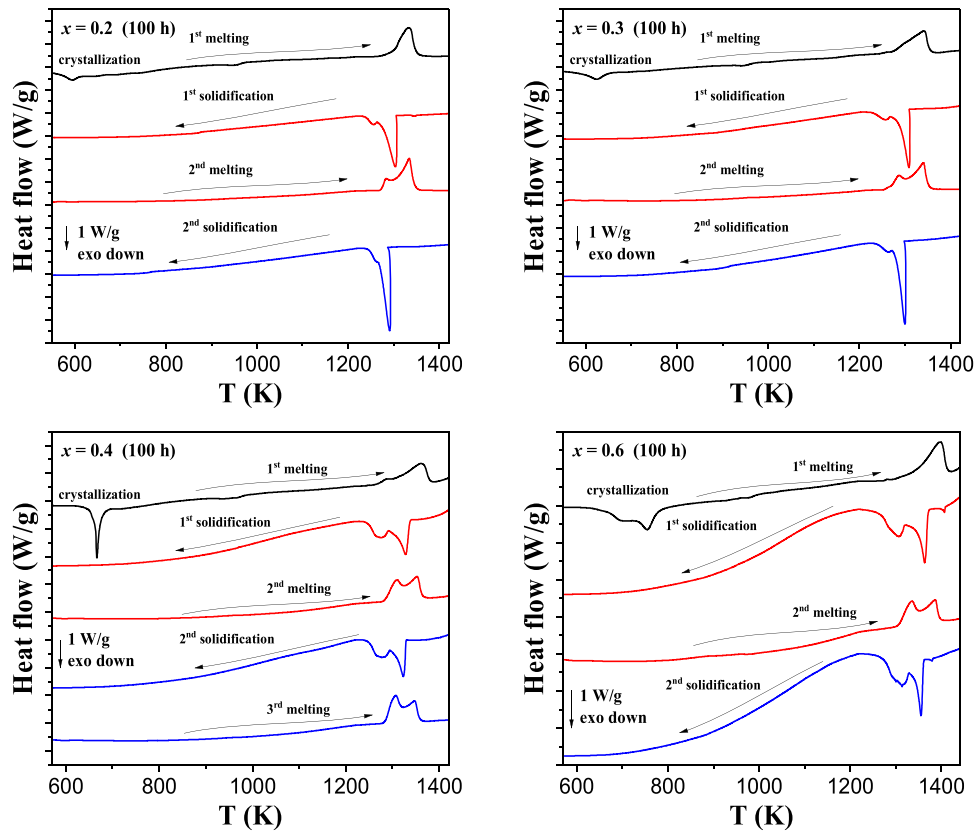Furthermore, the exothermic peaks associated with the solidification

Fig. 5. Subsequent DSC scans at 20 K/min from room temperature to 1673 K and then cooling down at 20 K/min to room temperature again for different Si content (scans below 600 K and above 1400 K do not present any transformation events). The vertical arrow indicates the magnitude and nature of the transformation.

process consistently reveal two distinct events for all the compositions under study. This observation indicates that the products following solidification at 20 K/min differ from those obtained in the final samples resulting from the annealing of mechanical alloys. In fact, the presence of a second melting process becomes evident, characterized by two endothermic peaks, and this phenomenon persists throughout subsequent solidification and melting cycles. As exemplified by $x = 0.4$ in Fig. 5, it even extends to a third melting process.

Fig. 6 presents XRD patterns at room temperature for the samples obtained by cooling the liquid in the calorimeter at a rate of 20 K/min for all the studied samples. In contrast to the final samples depicted in Fig. 2, the samples obtained after melting exhibit the coexistence of up to three phases: the martensitic and austenitic phases, along with a body-centered cubic (bcc) solid solution. It becomes evident that an increase in Si content stabilizes the martensitic orthorhombic phase, whereas lower Si content predominantly stabilizes the austenitic phase. The cell volume of each phase decreases with increasing Si content, as also illustrated in Fig. 4 for the austenitic phase.

3.3. Magnetocaloric effect

These alloys are of significant interest due to their MCE, which can be explored through isothermal specific magnetization curves at various temperatures, denoted as $\sigma(T, H)$. As an illustrative example, Fig. 7 presents the isothermal magnetization curves (7a and 7c) and the temperature dependence (7b and 7d) of magnetization for the final samples of $x = 0.4$ and x = 0.6 alloys, both milled for 100 h. In all the studied samples, the expected magnetization decay with temperature is observed as the Curie temperature is approached. Nevertheless, the behavior is slightly more intricate in the case of $x = 0.6$ due to the two-phase nature of this sample. This complexity is evidenced by the presence of two distinct peaks associated with the respective Curie

temperatures in the derivative of magnetization with respect to temperature (as shown in the inset of Fig. 7d) and is further corroborated by XRD analysis (see Fig. 2 for $x = 0.6$).

To characterize the MCE response of the samples, the specific magnetic entropy change, Δs_m, can be calculated using the Maxwell relation [21], which is related to the temperature derivative of specific magnetization, σ:

$$\Delta s_m(T, H_{max}) = \mu_0 \int_0^{H_{max}} \left(\frac{\partial \sigma}{\partial T}\right)_H dH, \tag{1}$$

Here, μ_0 represents the permeability of vacuum, T stands for temperature, and H corresponds to the magnetic field with $\mu_0 H_{max} = 1.5$ T. The results are presented in Fig. 8 for all the studied samples.

Concerning the magnitude and nature of the MCE responses, significant differences exist between samples exhibiting a first-order phase transition (FOPT) or a second-order phase transition (SOPT). Generally, it is observed that the values of Δs_m for samples with a FOPT [1,7,22–24] are higher than those for samples with a SOPT [5,14,20,25–27]. However, it is important to note that samples with a FOPT exhibit a hysteresis phenomenon, and the sharp character of Δs_m limits these significant values to a relatively small temperature range around the transition temperature. Consequently, samples with a SOPT offer advantages such as negligible magnetic and thermal hysteresis phenomena and broader peaks.

While Δs_m is commonly used to characterize the MCE response, the most crucial parameter is the adiabatic temperature change, ΔT_{ad} [21]. Measuring ΔT_{ad} experimentally can be challenging due to the adiabatic conditions required. However, ΔT_{ad} can also be related to magnetization results as follows [27]:
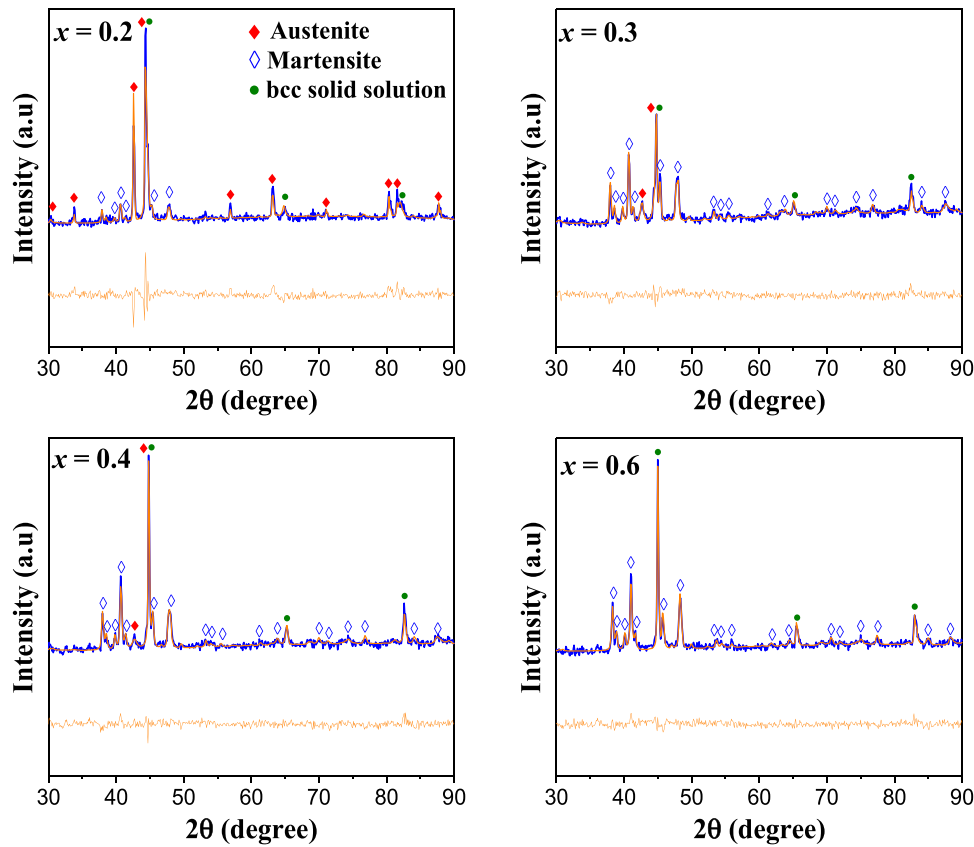
Fig. 6. XRD patterns of samples milled 100 h melting several times for different Si content. The experimental data are shown in blue, and the Rietveld fittings in orange. The differences between the experimental data and the Rietveld fittings are shown in orange below each experimental pattern.

$$\Delta T_{ad}(T, H_{\max}) = -\mu_0 \int\limits_0^{H_{\max}} \frac{T}{c_{p,H}} \left(\frac{\partial \sigma}{\partial T}\right)_H dH, \tag{2}$$

Here, $c_{p,H}$ represents the specific heat at constant pressure, which is a function of both temperature and magnetic field. As $c_{p,H}$ decreases (increases) with the applied field for $T < T_C$ ($T > T_C$), one can estimate a minimum (maximum) value of ΔT_{ad} by assuming the zero-field value, $c_{p,0}$, below and above the Curie temperature. Consequently, a relationship between Δs_m and ΔT_{ad} can be derived by comparing Eqs. (1) and (2):

$$\Delta T_{ad}(T, H_{\max}) \approx \frac{T\Delta s_m(T, H_{\max})}{c_{p,0}(T)}. \tag{3}$$

Figs. 9a and 9b illustrate the temperature dependence of zero-field specific heat and the thermodynamic estimation of ΔT_{ad} for the alloys exhibiting the highest MCE response among those studied here ($x = 0.4$ and 0.6). Fig. 9a reveals no thermal hysteresis between the cooling (circles symbols) and heating (squares) processes, indicating that these samples exhibit a SOPT. For the sample with $x = 0.4$, a specific heat peak is observed at ~275 K, consistent with the detected Curie temperature (as seen in Fig. 7). At T_C, a minimum value of $\Delta T_{ad} \geq 0.74 \pm 0.03$K is measured for this sample at an applied magnetic field value of $\mu_0 H = 1.5$ T.

For $x = 0.6$, despite the two-phase character of this sample, there is a specific heat peak at ~270 K, and no peak is observed around 335 K. This absence of the peak may be attributed to its broadening and overlap with the declining region of the preceding peak, as will be discussed further. Additionally, lower specific heat values are observed in this sample compared to those obtained for $x = 0.4$, followed by a sudden increasing trend at ~300 K. This experimental result is likely primarily attributed to the magnetic contribution of both phases. On one hand, the

fraction of austenite is lower, resulting in the lower values. On the other hand, the magnetic transition of the martensitic phase causes the observed increase in this temperature interval.

4. Discussion

Table 3 summarizes the relevant parameters of the magnetocaloric effect (Curie temperature, T_c; maximum magnetic entropic change in absolute value, $\Delta s_m^{\max}$; and refrigerant capacity, $RC = \Delta s_m^{\max} \cdot FWHM$, where FWHM represents the full width at half maximum of the $\Delta s_m vs. T$). It also includes some data from the literature on similar compositions for comparison. Among the samples studied in this work, the most remarkable MCE response is achieved by the sample with $x = 0.4$ milled for 100 h, which exhibits a Δs_m value of -1.39 ± 0.01 J·kg^{-1}·K^{-1}. This represents approximately a 25% improvement compared to the value of -1.12 ± 0.01 J·kg^{-1}·K^{-1} obtained for a sample with $x = 0$ milled for 100 h, as reported in reference [14].

As shown in Table 3, the evolution of the Curie temperature for the austenitic phase is influenced by both Si content and milling time. For the final samples obtained from a precursor milled for 30 h, the Curie temperature decreases as Si content increases. However, this trend deviates for the 50-hour milled precursor of $x = 0.6$, where the Curie temperature increases. For precursor milling times of 100 h, the Curie temperatures remain relatively constant as Si content increases, within the corresponding margin of error. In contrast, the evolution of Δs_m is more apparent, with the absolute value increasing as the milling time of the precursor system extends. Furthermore, for $x = 0.4$ and a 100-hour milling time, this magnitude reaches its maximum value among the samples studied in this work. The field dependence of the magnetic entropy change and refrigerant capacity can be expressed as power laws of the field, $\Delta s_m^{\max} \propto H^n$ [28] and $RC \propto H^m$ [29], respectively, where n and m are exponents that depend on the field and temperature. For
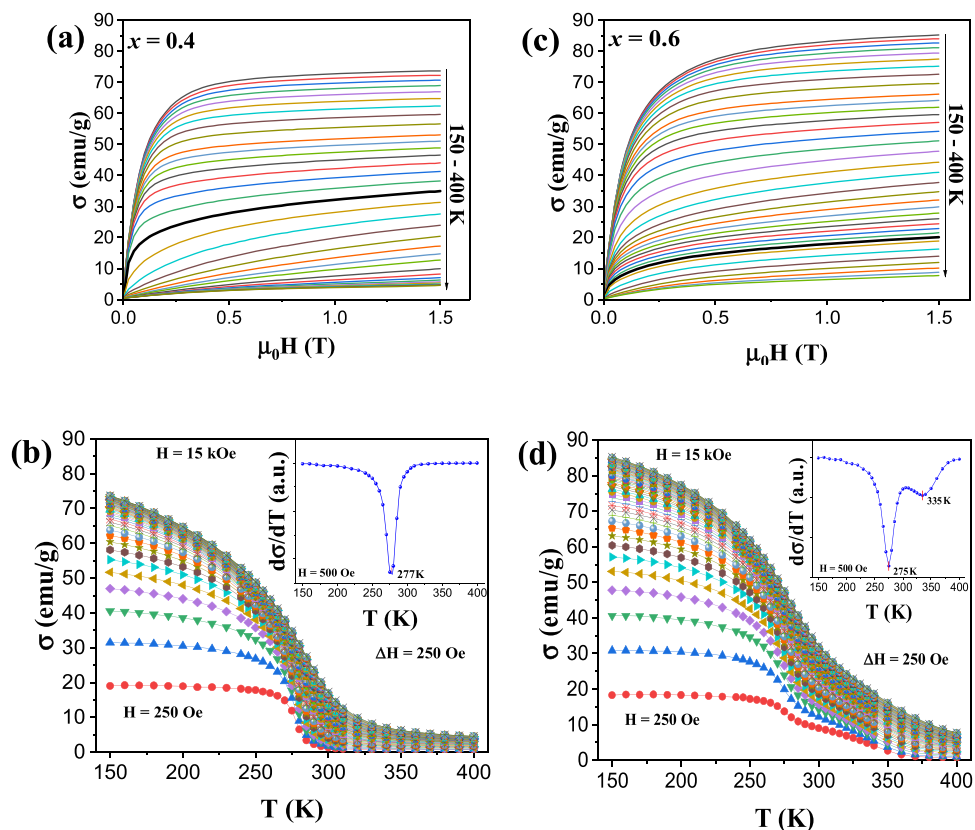
Fig. 7. Isothermal magnetization curves for the final samples with x = 0.4 (a) and x = 0.6 (c) milled 100 h, and the temperature dependence of the magnetization of these samples (b) and (d), respectively. The arrow in panels (a) and (c) indicates the temperature evolution. The thicker black line corresponds to the isothermal magnetization at the corresponding Curie temperatures. Temperature span, $\Delta T = 10$ K in the ranges 150–240 K and 340–400 K, and $\Delta T = 5$ K in the range 240–340 K. Magnetic field, $\mu_0 \Delta H$, span is 0.025 T between 0 and 1.5 T. The inset of (b) and (d) shows the $d\sigma/dT$ curves for a magnetic field of 0.05 T, and the temperature values of the peaks are indicated.
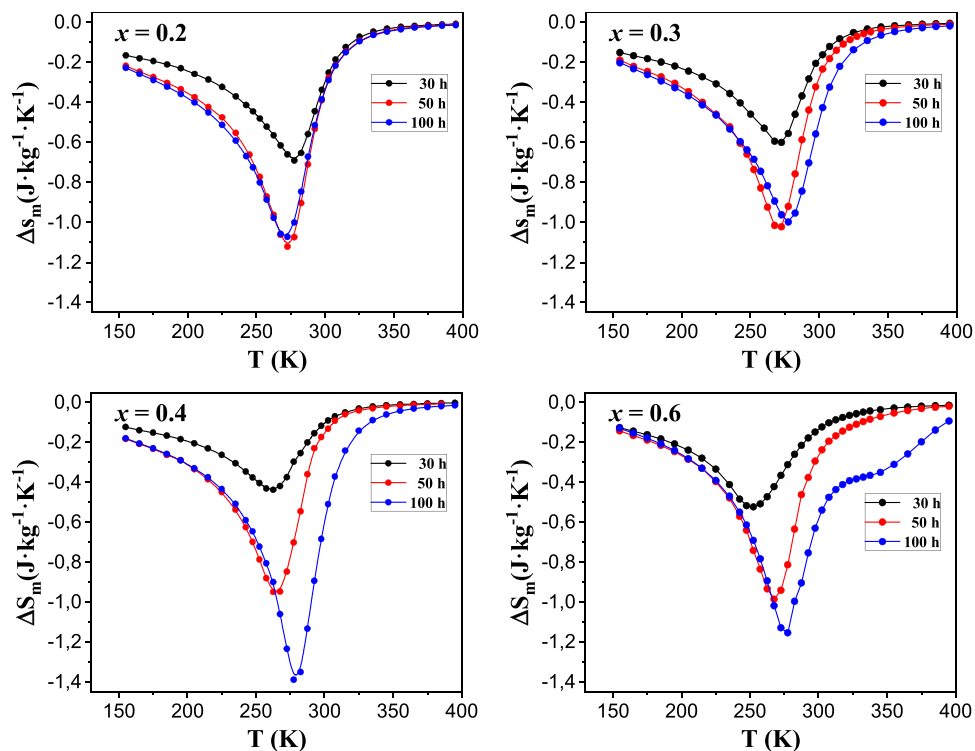

Fig. 8. Temperature dependence of $\Delta s_m(T)$ for x = 0.2, 0.3, 0.4 and 0.6 samples for different milling times and an applied magnetic field value of $\mu_0 H_{max} = 1.5$ T.
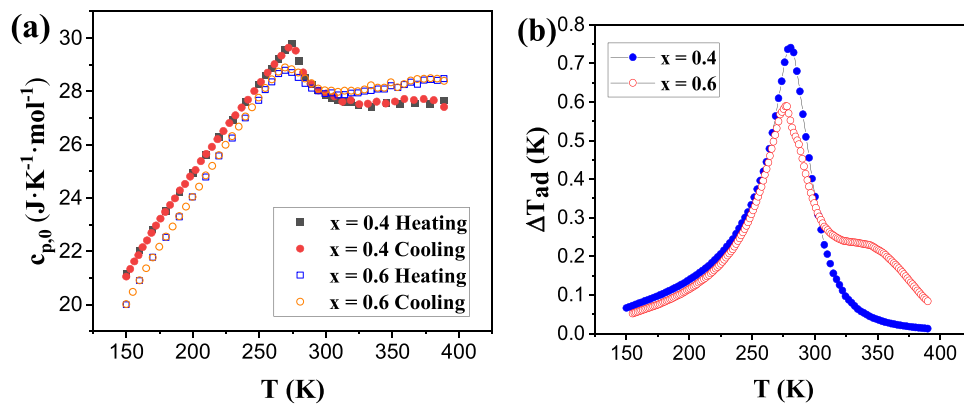
Fig. 9. Temperature dependence of specific heat, $c_{p,0}(T)$ **(a)**, and estimated adiabatic temperature change, $\Delta T_{ad}(T)$ **(b)** for an applied magnetic field value of $\mu_0 H_{max}$ = 1.5 T in MnCo$_{0.8}$Fe$_{0.2}$Ge$_{1-x}$Si$_x$ alloys milled 100 h at room temperature and then heated up to 723 K (x = 0.4) and 883 K (x = 0.6) at 20 K/min.

Table 3
Comparison of MCE parameters for different MnCoGe-based alloys (* sample with a FOPT).

Composition	Precursor synthesis	Thermal treatment	T_{pk} (K)	Δs_m^{max} (J·kg^{-1}·K^{-1})	RC (J·kg^{-1})	$\mu_0 \Delta H$ (T)	Δs_m^* (J·kg^{-1}·K^{-1})	RC^* (J·kg^{-1})	Ref.
MnCo$_{0.8}$Fe$_{0.2}$Ge$_{0.8}$Si$_{0.2}$	MA	723 K (20 K/min)	273(3)	-1.07(1)	69(1)	1.5	-3.04	291	This work
MnCo$_{0.8}$Fe$_{0.2}$Ge$_{0.7}$Si$_{0.3}$	MA	723 K (20 K/min)	278(3)	-1.00(1)	70(1)	1.5	-2.92	294	
MnCo$_{0.8}$Fe$_{0.2}$Ge$_{0.6}$Si$_{0.4}$	MA	723 K (20 K/min)	278(3)	-1.39(1)	65(1)	1.5	-3.69	289	
MnCo$_{0.8}$Fe$_{0.2}$Ge$_{0.4}$Si$_{0.6}$	MA	883 K (20 K/min)	275(3) (A) 335(3) (M)	-1.15(1)	64(1)	1.5	-3.70	302	
MnCo$_{0.8}$Fe$_{0.2}$Ge	MA	723 K (20 K/min)	272(3)	-1.01(1)	66(1)	1.5	-2.65	274	[14]
MnCo$_{0.94}$Fe$_{0.06}$Ge	MA	723 K (20 K/min)	279(3)	-1.02(1)	62(1)	1.5	-2.78	299	[20]
MnCo$_{0.97}$Fe$_{0.03}$Ge	MA	723 K (20 K/min)	275(3)	-1.05(1)	61(1)	1.5	-2.70	304	
MnCo$_{0.94}$Fe$_{0.06}$Ge	AM	1123 K (5 days)$_Q$	315	-27.5 *	-	5	-	-	[1]
MnCoGe$_{0.5}$Si$_{0.5}$	AM	1123 K (3 days)$_{IN}$	373	-4.4	282	5	-4.4	282	[25]
Mn$_{0.97}$Y$_{0.03}$CoGe	AM	1273 K (5 days)$_{OUT}$	296	-15.6 *	132.8	3	-	-	[22]
Mn$_{0.98}$Al$_{0.02}$CoGe	AM	1123 K (7 days)$_Q$	270.5	-3.21	242.2	5	-3.21	242.2	[26]
Mn$_{0.975}$Ni$_{0.025}$CoGe	AM	1123 K (5 days)$_Q$	270	-30.3 *	255.4	7	-	-	[23]
MnCo$_{0.96}$Cd$_{0.04}$Ge	AM	1173 K (7 days)$_Q$	330	-9.01	280.6	5	-9.01	280.6	[27]
MnCo$_{0.98}$Cu$_{0.02}$Ge	AM	1123 K (5 days)	271	-22.4 *	211.1	5	-	-	[24]
Mn$_{0.96}$Cr$_{0.04}$CoGe	AM	-	322	-28.5 *	-	5	-	-	[7]
MnCo$_{0.96}$Gd$_{0.04}$Ge	AM	1123 K (4 days)$_Q$	283 (A) 318 (M)	-3.0	296	5	-3.0	296	[5]

MA indicates mechanical alloying, **AM** arc-melting, **Q** quenching treatment, **IN** cooling inside the furnace, **OUT** cooling outside the furnace, **(A)** austenite phase and **(M)** martensite phase.

Table 4
Values of n and m exponents of samples milled 100 h.

Si content	n exponent, $\pm$ 0.01 ($\Delta s_m^{max} \propto H^n$)	m exponent, $\pm$ 0.001 ($RC \propto H^m$)
x = 0.2	0.87	1.196
x = 0.3	0.89	1.192
x = 0.4	0.81	1.242
x = 0.6	0.97	1.289

Mean field exponents values are: n = 0.67 and m = 1.33.

second-order phase transitions (SOPT), which are expected for the studied samples, both exponents are related to the material's critical exponents: $n = 1 + \frac{1}{\delta}\left(1 - \frac{1}{\beta}\right)$ and $m = 1 + \frac{1}{\delta}$, where β and δ are the critical exponents, and they are related to a third critical exponent, γ, as follows: $\delta = 1 + \frac{\gamma}{\beta}$ [28,29]. Using these relationships, it is possible to rescale the Δs_m and RC values for different magnetic fields if both exponents n and m are known, and the sample exhibits a SOPT:

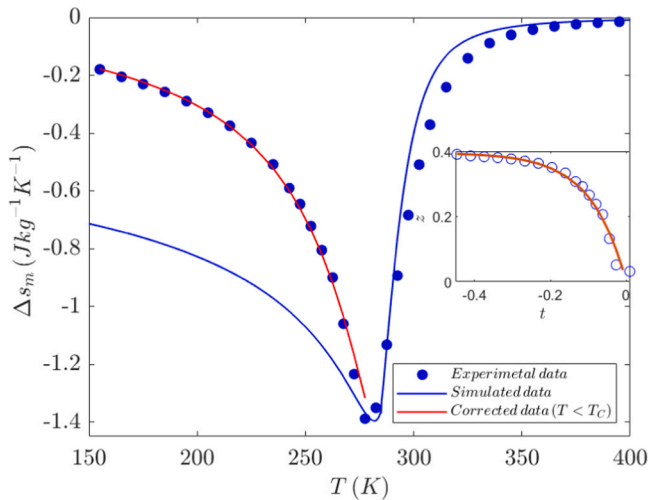$$\Delta s_m^*(H^*) = \Delta s_m(H) \cdot \left(\frac{H^*}{H}\right)^n, \tag{4}$$

Fig. 10. Temperature dependence of $\Delta s_m(T)$ for x = 0.4 sample (symbols), for an applied magnetic field of $\mu_0 H_{max} = 1.5$ T, compared with the simulated data obtained by means of the Arrott-Noakes equation of state (blue solid line) and phenomenological correction of the Arrott-Noakes deviation as T departs from T_C (solid red line). The inset shows this deviation for T < T_C and the red line in the inset corresponds to the fitting used in normalized units ($z = \left[\Delta s_M^{exp}(T) - \Delta s_M^{A-N}(T)\right]/\Delta s_M^{exp}(T_C)$ and $t = [T - T_C]/T_C$) build up the red curve of the main panel.
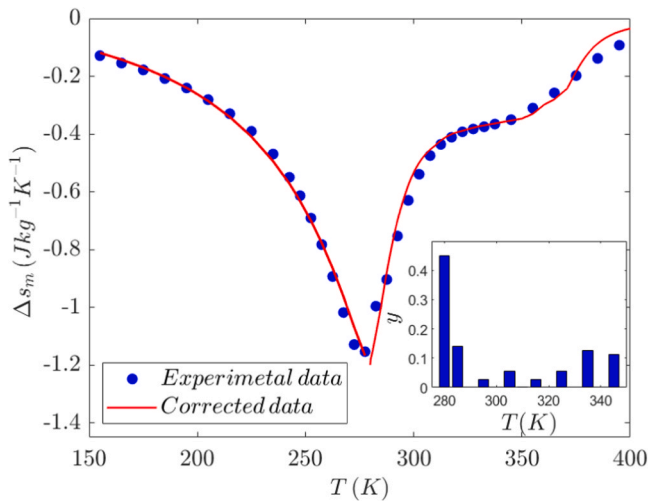

Fig. 11. Temperature dependence of experimental $\Delta s_m(T)$ for x = 0.6 sample (symbols), for an applied magnetic field value of $\mu_0 H_{max} = 1.5$ T, compared with the simulated data obtained by addition of the contributions indicated in the inset using the phenomenologically corrected Arrott-Noakes equation of state obtained for x = 0.4 (solid line).

$$RC^*(H^*) = RC(H) \cdot \left(\frac{H^*}{H}\right)^m, \qquad (5)$$

where Δs_m^* and RC^* are rescaled magnitudes for a magnetic field H^*. To facilitate comparison with literature data, it is necessary to rescale these values for a magnetic field of $\mu_0 H^* = 5$ T, for example. Since only two of the critical exponents are independent, in this work, exponents n and m have been calculated according to both power laws of the field (see Table 4), and the exponents β, γ and δ have been determined according to the relationships mentioned earlier. However, for the remaining samples listed in Table 3, mean field exponent values are assumed, i.e., n = 2/3 and m = 4/3. The values of Δs_m^* and RC^* with $\mu_0 \Delta H^* = 5$ T obtained in this study are compared with other MnCoGe-based materials

that show a SOPT, such as MnCoGe$_{0.5}$Si$_{0.5}$ [25], Mn$_{0.98}$Al$_{0.02}$CoGe [26], MnCo$_{0.96}$Cd$_{0.04}$Ge [27] and MnCo$_{0.96}$Gd$_{0.04}$Ge [5].

The optimal values of $\Delta s_m^* = -3.70$ J·kg^{-1}·K^{-1} and $RC^* = 380$ J·kg^{-1} obtained in this work correspond to the sample with x = 0.6. This sample is particularly intriguing because the FWHM value increases due to the coexistence of martensite and austenite phases with closely spaced Curie temperatures, 275 K and 335 K, respectively, resulting in an enhancement of RC. However, the coexistence of phases does not necessarily represent the optimal scenario for this rescaling. Large values of n are generally attributed to a broadening in the transition due to the presence of a distribution of Curie transitions [30]. Among the studied samples, this parameter is minimized for x = 0.4 (a single phase from a fully amorphous precursor) and maximized for x = 0.6 (a two-phase system).

To investigate the disparities between the mean field values of the exponents n and m and the higher values obtained in this study and to explore the relationship between the increase in RC and the phase coexistence in the sample with x = 0.6 milled for 100 h, the thermomagnetic response of a two-phase system with two Curie temperature distributions has been simulated using the Arrott-Noakes equation of state [31]:

$$\left(\frac{H}{\sigma}\right)^{\frac{1}{\gamma}} = a(T - T_C) + b\sigma^{\frac{1}{\beta}}, \qquad (6)$$

In this equation, the parameters a and b are related to the critical amplitudes of the isothermal initial susceptibility, the spontaneous magnetization and critical magnetization, the critical exponents (β, γ and δ), and Curie temperature T_C [32].

To achieve this, the thermomagnetic response of one phase with a SOPT in the magnetic field range up to a maximum value of $\mu_0 H = 1.5$ T in 10 mT increments, and in the temperature range from 150 K to 400 K in 0.1 K increments, was simulated according to Eq. (6) with the corresponding values of T_C, γ, β, b and a determined as follows: i) this phase has a Curie temperature value of $T_C = 280$ K (associated with the austenite phase; single phase in x = 0.4 and low-temperature phase in x = 0.6); ii) the critical exponents $\gamma = (2 - m)/(m - n)$ and $\beta = (m - 1)/(m - n)$ were determined after finding the exponents n and m, as discussed earlier (see Table 4); iii) the parameter b was determined through a nonlinear fit of the experimental critical magnetizations $\sigma(T = T_C, H) = \left(\frac{1}{b}\right)^{\gamma/\delta} H^{1/\delta}$, where $\delta = 1/(m - 1)$ (see black line in Fig. 7a); and finally, iv) the parameter a was obtained using the Kouvel-Fisher iterative method ($\sigma^{\frac{1}{\beta}}$ versus $\left(\frac{H}{\sigma}\right)^{\frac{1}{\gamma}}$), not shown here), fitting the linear behavior of the y-axis intercept values according to the expression $\left(\frac{H}{\sigma}\right)^{1/\gamma} = a(T - T_C)$, i.e., solving Eq. (6) using σ = 0. The results are presented in Fig. 10, and a good agreement is observed between the experimental data (sample with x = 0.4 milled for 100 h) and the simulated data around the phase transition temperature $T_C = 280$ K. An acceptable agreement above the Curie temperature is obtained because power laws are a fairly good approximation in this temperature range. However, a less satisfactory agreement is found below the Curie temperature, as expected, since the Arrott-Noakes equation of state does not accurately represent the thermomagnetic response in this temperature range. A phenomenological correction of the Arrott-Noakes deviations has been performed using the difference for T < T_C between the experimental data and the simulated ones, as shown in the inset of Fig. 10.

For x = 0.6, we assume a distribution of individual non-interacting contributions similar to that of x = 0.4, enabling the total magnetic entropy change to be expressed as a rule-of-mixture sum of the entropy changes of each constituent contribution. Consequently, the simulated specific magnetic entropy change, Δs_m, has been calculated using Eq. (1), where the specific magnetization, σ, is the sum of these contributions. The results are presented in Fig. 11, and they exhibit a favorable agreement between the experimental data (sample with x = 0.6 milled
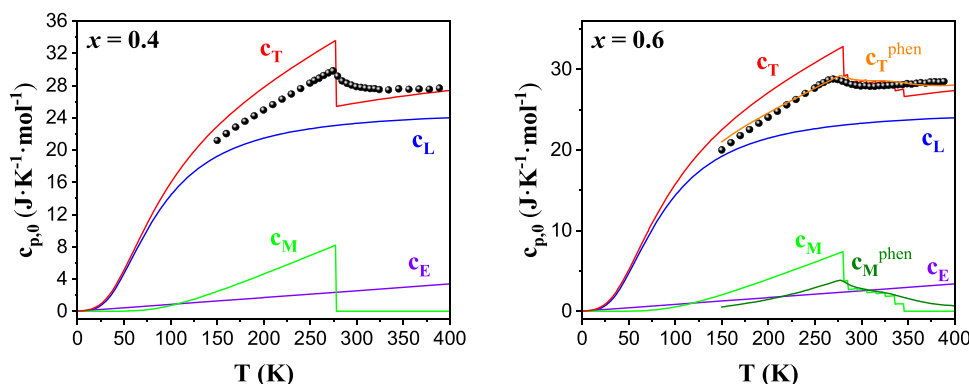
Fig. 12. Simulated temperature dependence of specific heat, $c_{p,0}(T)$ in in $MnCo_{0.8}Fe_{0.2}Ge_{1-x}Si_x$ alloys milled 100 h at room temperature and then heated up to 723 K ($x = 0.4$) and 883 K ($x = 0.6$) at 20 K/min, where experimental data are shown as black points and each specific heat contribution is shown as colored line (lattice contribution in blue, electronic contribution in purple, magnetic contribution in green, total contribution in red, magnetic phenomenological contribution in dark green and total phenomenological contribution in orange).

for 100 h) and the simulated data. Additionally, the fractions of the constituent contributions are displayed in the corresponding inset. The bimodal character of this histogram aligns with the presence of the two phases detected by XRD. Through the application of the phenomenological correction, it is possible to achieve a good agreement for temperatures both below and above the magnetic transition, as demonstrated in Fig. 11.

Finally, to demonstrate the reliability of the histogram in describing the behavior of the sample with $x = 0.6$, the total specific heat, $c_{p,0}$, has been simulated as:

$$c_{p,0}(T) = c_L + c_E + c_M, \tag{7}$$

Here, the subscripts L, E and M denote lattice, electronic, and magnetic contributions, respectively. The lattice and electronic contributions were simulated using a Debye temperature Θ of 353 K and a gamma factor γ of 8.44 mJ$^{-1}\cdot$K^{-2}, respectively, as reported in [33]. The magnetic contribution was simulated employing the Brillouin function with a Landé factor g of 2 and $J = 1/2$ per atom, inferred from a specific saturation magnetization of approximately ~70 emu/g (refer to Fig. 7). In Fig. 12, both the simulated and experimental specific heat curves are presented. Notably, no free parameters were employed in generating the theoretical curves depicted in red. For the $x = 0.6$ sample, the inset histogram in Fig. 11 was used to simulate the magnetic contribution in two distinct ways. On one hand, individual theoretical Brillouin functions yielded the red curve in Fig. 12. On the other hand, the phenomenological magnetic contribution of $x = 0.4$ was derived by subtracting c_L and c_E from the experimental data, and this c_M^{phen} was normalized to $t = (T - T_C)/T_C$ to propose individual phenomenological contributions, as indicated by the histogram in the inset of Fig. 11, resulting in the orange curve. It is worth mentioning that a good agreement is obtained, taking into account that no free parameters were utilized in this data simulation.

5. Conclusions

Amorphous precursor samples of $MnCo_{0.8}Fe_{0.2}Ge_{1-x}Si_x$ (with $x = 0.2$, 0.3, 0.4, and 0.6) were synthesized using the mechanical alloying technique. Microstructural analysis via XRD revealed partial amorphization in these systems. Upon thermal treatment, various phases were developed, with austenite phases predominant in low Si content samples, while samples with the highest Si content displayed a mixture of austenite and martensite phases.

The stability of mechanically alloyed precursors was assessed through DSC experiments, with the amorphous phase found to remain stable up to 973 K. However, subsequent melting processes resulted in transformations that differed from the initial solidification.

The most significant MCE response was observed in the sample with $x = 0.4$, milled for 100 h, which exhibited $\Delta s_m = -1.39 \pm 0.01$ J·kg^{-1}·K^{-1} and $\Delta T_{ad} \geq 0.74 \pm 0.03$ K for a maximum magnetic field change of $\mu_0 \Delta H = 1.5$ T. Additionally, the sample with $x = 0.6$ was of interest due to the increased FWHM resulting from the coexistence of martensite and austenite phases with similar Curie temperatures, enhancing the RC compared to single-phase systems.

The presence of a distribution of different Curie temperatures is consistent with magnetic and specific heat measurements, which were successfully simulated using the Arrott–Noakes equation of state and phenomenologically corrected at temperatures away from the Curie transition.

CRediT authorship contribution statement

A. Vidal-Crespo: Conceptualization, Formal analysis, Investigation, Writing – original draft, **R. Caballero-Flores**: Conceptualization, Methodology, Investigation, Resources, Writing – review & editing, **J.J. Ipus**: Conceptualization, Methodology, Investigation, Resources, Writing – review & editing, **J.S. Blázquez**: Conceptualization, Methodology, Investigation, Resources, Writing – review & editing, Supervision, **F.J. Romero**: Methodology, Resources, Writing – review & editing, **C.F. Conde**: Methodology, Resources, Writing – review & editing, Supervision.

Declaration of Generative AI and AI-assisted technologies in the writing process

During the preparation of this work the authors used ChatGPT-OpenAI in order to improve the language. After using this tool/service, the authors reviewed and edited the content as needed and take full responsibility for the content of the publication.

Declaration of Competing Interest

The authors declare that they have no known competing financial interests or personal relationships that could have appeared to influence the work reported in this paper.

Data availability

Data will be made available on request.

Acknowledgments

References

[1] G.J. Li, E.K. Liu, H.G. Zhang, Y.J. Zhang, J.L. Chen, W.H. Wang, H.W. Zhang, G. H. Wu, S.Y. Yu, Phase diagram, ferromagnetic martensitic transformation and magnetoresponsive properties of Fe-doped MnCoGe alloys, J. Magn. Magn. Mater. 332 (2013) 146–150, https://doi.org/10.1016/j.jmmm.2012.12.001.

[2] W. Jeitschko, A high-temperature X-ray study of the displacive phase transition in MnCoGe, Acta Crystallogr. Sect. B 31 (1975) 1187–1190, https://doi.org/10.1107/S0567740875004773.

[3] Y.-Y. Zhao, F.-X. Hu, L.-F. Bao, J. Wang, H. Wu, Q.-Z. Huang, R.-R. Wu, Y. Liu, F.-R. Shen, H. Kuang, et al., Giant negative thermal expansion in bonded MnCoGe-based compounds with Ni2In-type hexagonal structure, J. Am. Chem. Soc. 137 (2015) 1746–1749, https://doi.org/10.1021/ja510693a.

[4] Q. Ren, W. Hutchison, J. Wang, A. Studer, G. Wang, H. Zhou, J. Ma, S.J. Campbell, Negative thermal expansion of Ni-doped MnCoGe at room-temperature magnetic tuning, ACS Appl. Mater. Interfaces 11 (2019) 17531–17538, https://doi.org/10.1021/acsami.9b02772.

[5] Y. Li, L. Qin, X. Zhang, Achievement of reversible table-like magnetocaloric effect in MnCo1-XGdxGe alloys around room temperature, Mater. Lett. 326 (2022) 132975, https://doi.org/10.1016/j.matlet.2022.132975.

[6] A. Onaka, M. Onoue, R. Onodera, Y. Mitsui, K. Koyama, Magnetic and structural properties of Fe-substituted MnCoGe with Ni2In-type structure, J. Magn. Magn. Mater. 563 (2022) 170000, https://doi.org/10.1016/j.jmmm.2022.170000.

[7] N.T. Trung, V. Biharie, L. Zhang, L. Caron, K.H.J. Buschow, E. Brück, From single-to double-first-order magnetic phase transition in magnetocaloric Mn1-xCrxCoGe compounds, Appl. Phys. Lett. 96 (2010) 162507, https://doi.org/10.1063/1.3399774.

[8] G.H. Meng, O. Tegus, W.G. Zhang, L. Song, J.H. Huang, Structural and magnetic properties of MnCo1-xVxGe compounds, J. Alloy. Compd. 497 (2010) 14–16, https://doi.org/10.1016/j.jallcom.2010.03.004.

[9] J.L. Wang, P. Shamba, W.D. Hutchison, M.F. Md Din, J.C. Debnath, M. Avdeev, R. Zeng, S.J. Kennedy, S.J. Campbell, S.X. Dou, Ti substitution for Mn in MnCoGe – the magnetism of Mn0.9Ti0.1CoGe, J. Alloy. Compd. 577 (2013) 475–479, https://doi.org/10.1016/j.jallcom.2013.06.134.

[10] A. Aryal, A. Quetz, S. Pandey, T. Samanta, I. Dubenko, M. Hill, D. Mazumdar, S. Stadler, N. Ali, Magnetostructural phase transitions and magnetocaloric effects in As-cast Mn1-XAlxCoGe compounds, J. Alloy. Compd. 709 (2017) 142–146, https://doi.org/10.1016/j.jallcom.2017.03.149.

[11] J.B.A. Hamer, R. Daou, S. Özcan, N.D. Mathur, D.J. Fray, K.G. Sandeman, Phase diagram and magnetocaloric effect of CoMnGe1-XSnx alloys, J. Magn. Magn. Mater. 321 (2009) 3535–3540, https://doi.org/10.1016/j.jmmm.2008.03.003.

[12] Y. Song, S. Ma, F. Yang, Z. Zhang, Y. Zhang, H. Zeng, S. Ur Rehman, G. Feng, X. Luo, C. Chen, et al., Co-vacancy induced magneto-structural transformation in Co and Ge bidirectional-regulation MnCoGe systems, J. Alloy. Compd. 819 (2020) 153061, https://doi.org/10.1016/j.jallcom.2019.153061.

[13] J.-H. Chen, T. Poudel Chhetri, C.-K. Chang, Y.-C. Huang, D.P. Young, I. Dubenko, S. Talapatra, N. Ali, S. Stadler, The influence of hydrostatic pressure and annealing conditions on the magnetostructural transitions in MnCoGe, J. Appl. Phys. 129 (2021) 215108, https://doi.org/10.1063/5.0053671.

[14] A. Vidal-Crespo, J.J. Ipus, J.S. Blázquez, A. Conde, Obtaining magnetocaloric MnCo(Fe)Ge intermetallics from low temperature treatment of mechanically alloyed precursors, J. Magn. Magn. Mater. 514 (2020) 167127, https://doi.org/10.1016/j.jmmm.2020.167127.

[15] V. Franco, Determ. Magn. Entropy Change Magn. Meas.: Import. Meas. Protoc. (2014) 1–19.

[16] Q. Design, Physical property measurement system, Heat. Capacit. Option User's Man. (2000) 37.

[17] J.C. Lashley, M.F. Hundley, A. Migliori, J.L. Sarrao, P.G. Pagliuso, T.W. Darling, M. Jaime, J.C. Cooley, W.L. Hults, L. Morales, et al., Critical examination of heat capacity measurements made on a quantum design physical property measurement system, Cryog. (Guildf.) 43 (2003) 369–378, https://doi.org/10.1016/S0011-2275(03)00092-4.

[18] A.R. Miedema, P.F. de Châtel, F.R. de Boer, Cohesion in alloys — fundamentals of a semi-empirical model, Phys. B+C. 100 (1980) 1–28, https://doi.org/10.1016/0378-4363(80)90054-6.

[19] A. Vidal-Crespo, J.J. Ipus, J.S. Blázquez, A. Conde, Mechanical amorphization and recrystallization of Mn-Co(Fe)-Ge(Si) compositions, Metals 9 (2019) 534, https://doi.org/10.3390/met9050534.

[20] A. Vidal-Crespo, J.J. Ipus, J.S. Blázquez, C.F. Conde, On the order of magnetic transition in MnCo1-xFexGe (x = 0.20, 0.06 and 0.03) mechanical alloys, J. Alloy. Compd. 930 (2023) 167381, https://doi.org/10.1016/j.jallcom.2022.167381.

[21] V. Franco, J.S. Blázquez, J.J. Ipus, J.Y. Law, L.M. Moreno-Ramírez, A. Conde, Magnetocaloric effect: from materials research to refrigeration devices, Prog. Mater. Sci. 93 (2018) 112–232, https://doi.org/10.1016/j.pmatsci.2017.10.005.

[22] H. Imam, H.G. Zhang, W.J. Pan, B.T. Song, J.H. Shi, M. Yue, Magnetostructural transitions with a critical behavior in Y-Doped MnCoGe Compounds, Intermetallics 107 (2019) 53–59, https://doi.org/10.1016/j.intermet.2019.01.008.

[23] S. Yang, Y. Song, X. Han, S. Ma, K. Yu, K. Liu, Z. Zhang, D. Hou, M. Yuan, X. Luo, et al., Tuning the magnetostructural transformation in slightly Ni-Substituted MnCoGe ferromagnet, J. Alloy. Compd. 773 (2019) 1114–1120, https://doi.org/10.1016/j.jallcom.2018.09.266.

[24] X. Si, K. Zhou, R. Zhang, X. Ma, Z. Zhang, Y. Liu, Prediction of magnetocaloric effect and spontaneous magnetization in Cu-doped MnCoGe system, Mater. Res. Express 5 (2018) 126104, https://doi.org/10.1088/2053-1591/aae23a.

[25] J.W. Lai, Z.G. Zheng, R. Montemayor, X.C. Zhong, Z.W. Liu, D.C. Zeng, Magnetic phase transitions and magnetocaloric effect of MnCoGe1-xSix, J. Magn. Magn. Mater. 372 (2014) 86–90, https://doi.org/10.1016/j.jmmm.2014.07.035.

[26] X. Si, Y. Liu, W. Lei, J. Xu, W. Du, J. Lin, T. Zhou, X. Lu, Enhancement of curie temperature and transition temperature range induced by Al Doping in Mn1-XAlxCoGe, Solid State Commun. 247 (2016) 27–30, https://doi.org/10.1016/j.ssc.2016.06.011.

[27] X. Si, Y. Shen, X. Ma, S. Chen, J. Lin, J. Yang, T. Gao, Y. Liu, Field dependence of magnetic entropy change and estimation of spontaneous magnetization in Cd substituted MnCoGe, Acta Mater. 143 (2018) 306–317, https://doi.org/10.1016/j.actamat.2017.10.008.

[28] V. Franco, J.S. Blázquez, A. Conde, Field dependence of the magnetocaloric effect in materials with a second order phase transition: a master curve for the magnetic entropy change, Appl. Phys. Lett. 89 (2006) 222512, https://doi.org/10.1063/1.2399361.

[29] V. Franco, A. Conde, Scaling laws for the magnetocaloric effect in second order phase transitions: from physics to applications for the characterization of materials, Int. J. Refrig. 33 (2010) 465–473, https://doi.org/10.1016/j.ijrefrig.2009.12.019.

[30] D. Doblas, L.M. Moreno-Ramírez, V. Franco, A. Conde, A.V. Svalov, G. V. Kurlyandskaya, Nanostructuring as a procedure to control the field dependence of the magnetocaloric effect, Mater. Des. 114 (2017) 214–219, https://doi.org/10.1016/j.matdes.2016.11.085.

[31] A. Arrott, J.E. Noakes, Approximate equation of state for nickel near its critical temperature, Phys. Rev. Lett. 19 (1967) 786–789, https://doi.org/10.1103/PhysRevLett.19.786.

[32] R. Caballero-Flores, N.S. Bingham, M.H. Phan, M.A. Torija, C. Leighton, V. Franco, A. Conde, T.L. Phan, S.C. Yu, H. Srikanth, Magnetocaloric effect and critical behavior in Pr0.5Sr0.5MnO3: an analysis of the validity of the maxwell relation and the nature of the phase transitions, J. Phys. Condens. Matter 26 (2014) 286001, https://doi.org/10.1088/0953-8984/26/28/286001.

[33] E. Yüzüak, I. Dincer, Y. Elerman, I. Dumkow, B. Heger, S. Yuce Emre, Enhancement of magnetocaloric effect in CoMn0.9Fe0.1Ge alloy, J. Alloy. Compd. 641 (2015) 69–73, https://doi.org/10.1016/j.jallcom.2015.04.062.